Journal of *Marine Science and Engineering*

MDPI

Article

Numerical Simulation Analysis of Hydrodynamic Coupling Effects and Energy Conversion Efficiency of Dual-Float Wave Energy Converters

Dongqin Li [1], Yu Zhang [2,*], Jie Hu [1], Yanqing Yin [2], Bohan Wang [2] and Wenwen Chen [3]

[1] School of Naval Architecture and Intelligent Manufacturing, Jiangsu Maritime Institute, Nanjing 211199, China; mandy_ldq@163.com (D.L.)
[2] Ocean College, Zhejiang University, Zhoushan 316000, China
[3] School of Naval Architecture and Ocean Engineering, Jiangsu University of Science and Technology, Zhenjiang 212100, China
* Correspondence: zy103@zju.edu.cn

Abstract

This study examines the hydrodynamic performance and energy conversion mechanisms of a dual-float wave energy converter (WEC) to address the limitations of single-float WECs regarding energy capture efficiency and cost-effectiveness. A three-dimensional numerical wave tank is constructed utilizing computational fluid dynamics (CFDs) technology and STAR-CCM+ to simulate the dynamic response of the dual-float system under specific wave conditions characterized by a height of 0.1 m and a period of 1.5 s. The effects of a front-rear configuration with a quarter-wavelength spacing on the converter's power output, turbofan rotational characteristics, and heave motion are systematically analyzed. The results indicate that the wave-facing float attains a consistent rotational speed of 4 rad/s, exhibiting significant fluctuations in heave displacement and velocity. Conversely, the downstream float exhibits diminished motion amplitude, a constant rotational velocity of 2.5 rad/s, and curtailed power generation attributable to wave diffraction and energy shielding from the wave-facing float. The mutual hydrodynamic interference between the floats influences the total energy conversion efficiency, as evidenced by the dual-float system's array impact factor of 0.989. A parametric study covering multiple wave conditions and float spacing is supplemented to reveal the influence law of key parameters on system performance. This paper elucidates the fundamental mechanism of hydrodynamic coupling in dual-float arrays and offers a theoretical foundation and technical guidance for the optimal design and engineering application of arrayed WECs.

Keywords: dual-float system; wave energy converter; hydrodynamic performance; numerical simulation; array impact factor; flow field characteristics; computational fluid dynamics

Check for updates

Academic Editors: Eugen Rusu, Nastia Degiuli and Ivana Martić

Received: 5 February 2026
Revised: 4 March 2026
Accepted: 10 March 2026
Published: 12 March 2026

Copyright: © 2026 by the authors. Licensee MDPI, Basel, Switzerland. This article is an open access article distributed under the terms and conditions of the Creative Commons Attribution (CC BY) license.

1. Introduction

As the global energy transition intensifies, wave energy, a renewable marine energy source characterized by substantial reserves and consistent output, has emerged as a pivotal research focus within the renewable energy sector [1,2]. WECs are essential apparatus for harnessing wave energy, and their efficacy directly influences the technical viability and economic advantages of wave energy usage [3,4]. Numerical simulation, particularly viscous CFD technology, has emerged as the fundamental technical approach for analyzing the hydrodynamic performance of WECs and optimizing array layouts. Comprehensive

academic evaluations and engineering methodologies have confirmed its dependability in recording intricate wave-structure interaction phenomena in marine renewable energy research [5,6]. Single-float WECs are constrained by their narrow energy capture range and inadequate structural stability, hindering efficient energy conversion in complex marine environments [7,8]. Consequently, arrayed WEC systems consisting of numerous floats have been a predominant development trend, since the synergistic interaction among floats may substantially enhance energy capture efficiency and structural reliability [9]. A judicious array layout can enhance energy capture efficiency and significantly diminish the hydroelastic response of floating WEC systems subjected to intricate wind-wave-current forces, hence augmenting the long-term structural integrity and energy harvesting consistency of the device [5,10].

The dual-float system, as a fundamental type of arrayed WECs, has garnered significant interest owing to its uncomplicated design and notable interaction effects. In contrast to single-float devices, dual-float systems can expand the frequency range of energy harvesting through hydrodynamic interference between floats, thus improving adaptability to intricate sea conditions [11]. However, the hydrodynamic behavior of dual-float systems is highly complex due to the diffraction, radiation, and flow field coupling effects between the two floats [12]. These processes entail significant nonlinear wave diffraction, multi-body flow field interactions, and vortex shedding around floating structures, which cannot be precisely characterized by conventional linear potential flow theory; thus, viscous numerical models are necessary for detailed simulation and quantitative analysis [13]. For example, the wave shielding effect of the front float may mitigate the motion response of the rear float, whereas gap resonance between floats can lead to localized energy concentration, impacting the structural integrity and energy conversion efficiency of the system [14]. Gao et al. confirmed that gap resonance can significantly alter hydrodynamic forces on structures, with the resonant wave height closely associated with structural factors like body draft and gap width [15]. Systematic review studies have established that float spacing and structural geometry dimensions are the primary parameters governing hydrodynamic interference effects, which directly influence the overall energy conversion efficiency and structural integrity of dual-float WEC systems [16]. Consequently, comprehensive investigation of the hydrodynamic properties of dual-float WECs is essential for enhancing their design and engineering implementation.

Current research on the hydrodynamic efficacy of WECs has established a robust foundation. CFD technology can precisely simulate nonlinear wave propagation, floating motion responses, and flow field intricacies, rendering it an ideal instrument for examining wave-structure interactions [17–19]. The SST k-ω turbulence model has been extensively validated for its exceptional efficacy in simulating wave-structure interactions and free surface evolution issues. Additionally, the weakly coupled fluid–structure interaction method, which incorporates modal superposition and Lagrangian CFD, offers an efficient and highly accurate solution for calculating the dynamic responses of floating WEC structures [5,13,20]. In experimental research, physical model tests can yield critical data, such as float motion responses, mooring forces, and energy output, which are vital for validating numerical models [11,21,22].

Nevertheless, contemporary research exhibits notable limitations: the majority of studies concentrate on the performance enhancement of individual float devices or the overarching properties of extensive arrays, whereas detailed investigations into dual-float systems remain inadequate. The quantitative investigation of hydrodynamic interference between dual floats is insufficiently detailed, and the methods by which layout factors affect energy conversion efficiency remain ambiguous [23,24].

This study aims to address the identified research gaps by examining the dual-float WEC system configured in a fore-and-aft layout. A three-dimensional numerical wave tank is developed using CFD technology to systematically investigate the dynamic response, flow field characteristics, and energy conversion efficiency of the system under defined wave conditions. An analysis of heave displacement, velocity fluctuations, turbine rotation characteristics, and flow field pressure distribution of the dual floats elucidates the inherent process of hydrodynamic interference between the floats. The impact of critical parameters, including float spacing and structural dimensions, on system performance is examined to offer a theoretical foundation and technical guidance for the optimal design of dual-float WECs. The research findings are anticipated to establish a basis for the optimization of layouts and engineering applications of arrayed WECs, hence facilitating the extensive advancement of wave energy utilization technology.

2. Design of the Dual-Float WEC

2.1. Design Ideas for the New WEC

Figure 1 depicts the dual-float WEC as a decentralized marine clean energy node, integrating with various offshore and subsea technologies to facilitate self-sufficiency in isolated marine environments [25]. Located in coastal or offshore waters, the converter tackles the issue of dependable energy access for systems beyond terrestrial grid connectivity. It offers a consistent, localized power supply for islands and reefs, replacing expensive fossil fuel supplies or unreliable solar alternatives. Amphibious robotic systems utilize it as a charging relay to prolong mission durations without the need for onshore recovery. Surface vessels utilize it as auxiliary power for equipment, diminishing dependence on onboard fuel supplies. Subsea artificial habitats utilize their consistent output to maintain life support and sensor equipment, thereby circumventing the limitations of battery replacement. Autonomous underwater vehicles dock at the converter to prolong operational durations for activities like pipeline inspections, while subsea oil and gas infrastructures and pipeline systems utilize it for decentralized monitoring power, hence avoiding the expenses associated with long-distance subsea cabling. This configuration emphasizes two principal features of the converter: its adaptability to diverse power requirements (ranging from low-power sensing to moderate-power charging) and its ability to facilitate self-sufficiency in areas lacking conventional infrastructure. In contrast to single-application systems, it prioritizes interoperability, in line with the architecture of next-generation marine renewable energy. It also diminishes the environmental impact of marine activities by decreasing dependence on fossil fuels in vulnerable environments.

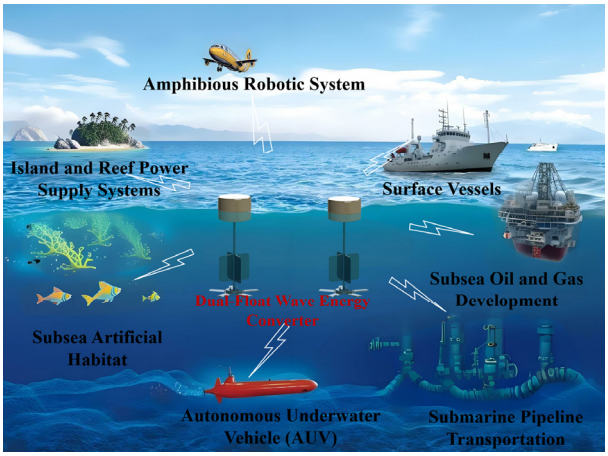


Figure 1. In situ energy supply technology for WECs.

The dual-float WEC proposed in this work features a fore-and-aft configuration, with both floats positioned perpendicular to the direction of wave propagation. This design incorporates cylindrical floats with Wells turbine blades to optimize the energy conversion process and minimize intermediate losses. This arrangement, unlike side-by-side layouts, reduces imbalanced lateral forces like sway and roll under oblique waves, limiting principal motion responses to heave and surge. This limitation reduces the complexity of power take-off system design while maintaining steady energy collection efficiency. The system comprises cylindrical floats, turbofans, transmission elements, permanent magnet brushless DC generators, damping plates, and mooring components. The primary design objective is to facilitate effective coupling between float heave motion and turbofan rotation, while maintaining structural integrity and adaptability to offshore wave conditions. As illustrated in Figure 2 [26], this converter harnesses and transforms wave energy via its distinctive structure and transmission features. Figure 2a shows the overall schematic of the device; Figure 2b presents the exploded view of the device's internal structure. When waves impact the float, it experiences heave motion, converting wave energy into linear mechanical energy. This motion, conveyed through a rigid sleeve connection to the turbofan, generates unidirectional fan rotation due to hydrodynamic forces, thereby transmitting mechanical energy. The rotating fan blades propel a coaxial shaft to rotate uniformly in one direction, which engages the terminal generator through a gear train. This transmission system ultimately converts rotational mechanical energy into electrical energy.

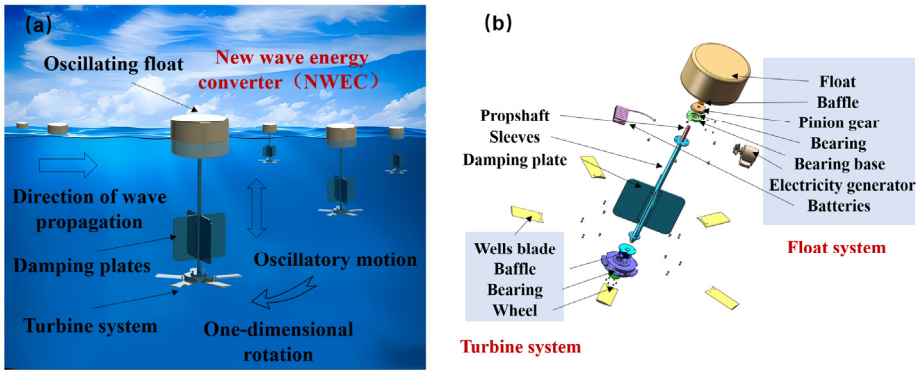


Figure 2. Design and energy conversion mechanisms of a novel type WEC. (**a**) Overall schematic diagram of the device; (**b**) exploded view of the device's internal structure.

Float spacing is a crucial parameter that regulates hydrodynamic interactions, such as diffraction, radiation, and gap resonance. For offshore wave conditions with a significant wave height of 0.1 m and a peak period of 1.5 s, the wavelength is determined to be 3.3789 m using the linear wave dispersion relation. The float spacing is established at one-quarter wavelength (0.8447 m) to balance hydrodynamic coupling effects and structural integrity. This positioning situates the rear float within the constructive interference zone of the front float's diffracted waves, while circumventing narrow-gap resonance.

The numerical wave tank is established via CFD method to systematically investigate the hydrodynamic performance of the dual-float WEC. The computational domain for numerical simulation is configured to span three wavelengths, resulting in a total length of 10.1367 m. The inlet boundary is positioned one wavelength from the origin, while the outflow boundary is situated two wavelengths from the origin. The domain possesses a width of 2.56 m, a height of 2.08 m, a water depth of 1 m, and 1.08 m of clearance over the sea surface. Wave generation employs the boundary condition method with Stokes fifth-order waves to model nonlinear propagation. A damping dissipation zone is implemented at the exit to avert wave reflection interference.

Each float utilizes a hollow sealed cylindrical design, chosen for its symmetrical hydrodynamic efficiency, ease of production, and low wave resistance. The principal dimensions comprise a diameter of 0.18 m, a height of 0.12 m (including both draft and freeboard), and a diameter-to-height ratio of 1.5:1. These dimensions achieve a balance among buoyancy, structural integrity, and responsiveness to heave action. The float is made of glass fiber-reinforced plastic with a density of 1400 kg/m^3, ensuring adequate buoyancy without significant inertia. The internal cavity contains the generator and transmission mechanism, along with designated areas for couplings and bearings.

The turbofan, fundamental to the power take-off system, employs NACA0015 symmetric airfoils to facilitate unidirectional rotation in reciprocating water flow. The parametric optimization of the blade count, chord length, and hub radius concludes with a design comprising five blades, a chord length of 0.05 m, a hub radius of 0.05 m, and a hub thickness of 0.03 m. This design balances torque output and flow resistance. A sturdy stainless-steel sleeve, featuring an inner diameter of 0.03 m and a wall thickness of 3 mm, links the turbofan to the float. This connection guarantees a uniform dynamic response and safeguards interior components from corrosion. Four rubber damping plates, each measuring 0.16 m in height, 0.1 m in width, and possessing a damping coefficient of 0.8 N·s/m, are symmetrically affixed around the sleeve. These plates augment structural stability and mitigate lateral vibrations, without contributing to energy transmission.

The generator is a permanent magnet brushless DC device with a rated power of 50 W, compatible with the system's output range. It attains an actual energy conversion efficiency of 72–78% at the rated operating speed of 4 rad/s (38 rpm) and features a compact design conducive to integration within the float. It is linked to the turbofan shaft using a 1:1 transmission ratio coupling, thereby eliminating energy waste from gear transfer. The linear damping coefficient of the power take-off system is set to 8 N·s/m, optimizing the heave amplitude of the floats and the efficiency of energy capture. This configuration mitigates fatigue caused by excessive movement and underperformance resulting from excessive damping.

The energy conversion process occurs in three steps. Initially, wave energy is harnessed by the floats. Secondly, mechanical energy is conveyed via the turbofans. Third, electrical energy is transformed by the generators. When waves impact the system, the front float first exhibits heave motion, causing the turbofan to rotate unidirectionally through reciprocating water flow. The rear float then experiences heave motion due to the interaction of incident and diffracted waves, hence augmenting total energy acquisition. The symmetric airfoil configuration guarantees that the turbofan sustains unidirectional rotation irrespective of the water flow direction. The generator transforms rotating mechanical energy into electricity, while linear damping calibrates the turbofan's resistance torque to align with the float's motion response. This adjustment optimizes the efficiency of wave energy capture.

2.2. Principle of Wave Energy Conversion

Structural elasticity and rigid-flexible coupling effects are key factors influencing energy extraction. Although flexible blades were initially considered for the rotating components, reliability concerns led to the adoption of rigid components for the entire device. Nonetheless, the design analysis highlighted the multi-body coupling interactions between the floater and the rotating blades. The structured configuration of the device is suitable for extensive application while enhancing power conversion efficiency. Arraying represents the forthcoming research trend in wave energy generation technology, and this work examines the comprehensive hydrodynamic response of the device based on various array configurations.

The energy conversion process of the NWEC involves the wave energy capture efficiency η_{cap} of the floats, the hydrodynamic efficiency η_{hyd} of the turbofan, and the power generation efficiency η_{gen} of the generator. The overall efficiency η of the WEC can be expressed as follows [8,27]:

$$\eta = \eta_{cap} \cdot \eta_{hyd} \cdot \eta_{gen} \tag{1}$$

The mechanical and electromagnetic relationship is a complex interaction, which is intensely influenced by nonlinear factors.

Vortex fan input power P_{input} is expressed in terms of the kinetic energy of the fluid that passes through the horizontal cross-section of the Wells blades per unit time:

$$P_{input} = \frac{E_{input}}{t} = \frac{\frac{1}{2}\rho(\pi R^2)hV_A^2}{t} = \frac{1}{2}\rho\pi R^2 V_A^3 \tag{2}$$

where E_{input} is the kinetic energy of a cylindrical fluid of height h and radius R passing through the horizontal cross-section of the fan blade at time t. V_A is the relative flow velocity of the fluid to the horizontal cross-section of the vortex fan. Where $V_A = h/t$, h is the height of the cylindrical fluid passing through the horizontal cross-section of the fan blade, and t is the corresponding action time, A is the cross-sectional area of the fan blade.

The output power of the vortex fan P_{output}:

$$P_{output} = T \cdot \omega = N \cdot T_{blade} \cdot \omega \tag{3}$$

where T is the output torque of the vortex fan, ω is the rotational velocity (rad/s), N is the number of blades the vortex fan has, and T_{blade} is the torque generated by a single blade on the drive shaft.

Wave energy array impact factor q is an important index to measure the characteristics of wave energy arrays, mainly considering the power generation of wave energy generating devices by the hydrodynamic interference between the array devices. Assuming that the array field consists of N identical power generators, the wave energy array impact factor q can be expressed as follows:

$$q = \frac{P_{total}}{N \cdot P_{single}} \tag{4}$$

where P_{total} is the total power generated by the wave energy array composed of N float-type wave energy generators, which is the sum of P_{output} of each float in the array; P_{single} is the output power of a single-float-type wave energy generator operating without hydrodynamic interference, which is consistent with the physical connotation of P_{output} defined in Equation (3).

If q is greater than 1, it means that the array arrangement improves the overall energy capture efficiency of the wave energy generator, and the array plays a positive role in improving the efficiency of wave energy utilization; if q is less than 1, it means that the array arrangement reduces the overall energy capture efficiency of the WEC, and the array plays a negative role in the utilization of wave energy. The magnitude of the impact factor is contingent upon the wave environment and the configuration of the wave energy device array. The configuration of the device array technique can be modified to ensure that the overall power produced by the array of power-producing devices exceeds the cumulative power of the individual float wave energy generating devices. The array impact of the novel float-type wave energy generator encompasses numerous variables, and its hydrodynamic features will be examined through a synthesis of theoretical analysis and numerical simulation.

2.3. Wave Mechanics Theory

The sum of kinetic and potential energy possessed by ocean surface waves is called wave energy. The total energy of a traveling wave stretching to infinity at both ends is infinite, and this section analyses the energy of a wave in one wavelength per unit width. The gravitational potential energy of the fluid in the volume microelement dxdy is $\rho g y \mathrm{d}x\mathrm{d}y$ (Figure 3).

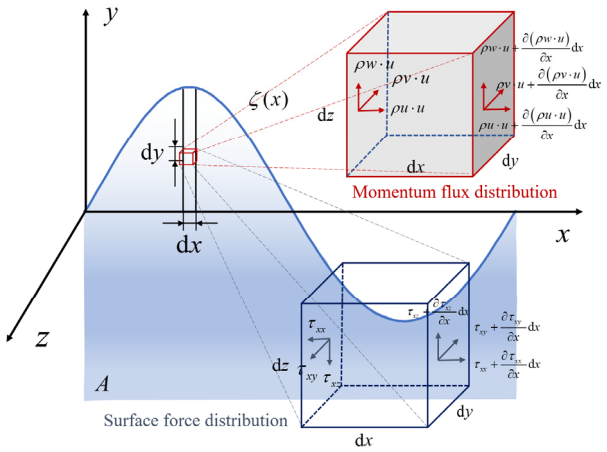


Figure 3. Surface force/momentum and energy analysis of a differential control volume over a wave period.

The momentum theorem in the x-axis can be expressed as:

$$\frac{\partial(\rho \cdot u)}{\partial t} + \frac{\partial(\rho \cdot u^2)}{\partial x} + \frac{\partial(\rho \cdot u \cdot v)}{\partial y} + \frac{\partial(\rho \cdot u \cdot w)}{\partial z} = F_x + \frac{\partial \tau_{xx}}{\partial x} + \frac{\partial \tau_{yx}}{\partial y} + \frac{\partial \tau_{zx}}{\partial z} \tag{5}$$

The gravitational potential energy for one wavelength is:

$$E_g = \int_0^{\lambda} \int_3^{\zeta} \rho g y \mathrm{d}x\mathrm{d}y = \frac{1}{2}\rho g \int_0^{\lambda} \zeta^2 \mathrm{d}x \tag{6}$$

where $\zeta = Ae^{i(mx-\omega t)}$ is the wavefront displacement.

In the spinless flow field of a given incompressible fluid, the fluid kinetic energy is:

$$E = \frac{\rho}{2} \iiint_{\tau} \nabla(\phi \nabla \phi) \mathrm{d}\tau = \frac{\rho}{2} \oiint_{A} \phi \nabla \phi \vec{n} \mathrm{d}s = \frac{\rho}{2} \oiint_{A} \phi \frac{\partial \phi}{\partial n} \mathrm{d}s \tag{7}$$

For this potential flow fluid kinetic energy formula applied to WEC research, the symbols are concisely defined in a single coherent description: E is the total fluid kinetic energy within the control volume τ (the numerical wave tank's fluid domain), the core metric for calculating WEC energy capture efficiency; ρ is seawater density; ϕ is the velocity potential, where fluid velocity satisfies $u = \nabla\phi$ in irrotational flow, forming the basis for wave generation and float-wave interaction analysis; ∇ is the 3D Hamiltonian differential operator for gradient and divergence calculations; A is the closed boundary of τ, covering the tank's inlet/outlet, walls and the floats' wetted surfaces.

In addition, the flow field has kinetic energy due to the motion of the fluid mass, and the kinetic energy per unit width of the wave is:

$$E_k = \frac{1}{2}\rho \iint_{s} \phi \frac{\partial \phi}{\partial n} \mathrm{d}s \tag{8}$$

The total energy of the wave, irrespective of surface tension, is the sum of gravitational potential energy and kinetic energy. The total energy is:

$$E = E_g + E_k = \frac{1}{2}\rho g A^2 \lambda \quad (9)$$

3. Numerical Simulation of Hydrodynamic Performance of Front and Rear Parallel Double Float WECs

3.1. CFD Simulation Settings

Overset mesh technique is utilized for numerical simulation. The domain comprises background structured grids of 0.02 m and locally refined overlapping unstructured grids with a minimum size of 0.005 m surrounding the floats and turbofans. The overall number of grids is roughly 1 million, optimizing computing precision and efficiency. Simulations utilize the STAR-CCM+ platform, incorporating three-dimensional spatial configurations, implicit unsteady time stepping, the Eulerian multiphase flow model employing the volume of fluid method for free surface representation, the k-ε turbulence model for turbulent flow dynamics, and gravity and volume of fluid wave models for wave generation and propagation. In this study, only the heave single degree of freedom of the float is released, and the other 5 degrees of freedom (sway, surge, roll, pitch, yaw) are constrained, to focus on the heave motion which is the core of wave energy capture, and reduce the interference of lateral motion on the power take-off system. A time step of 0.005 s is chosen to guarantee precision in transient motion and flow field simulation. Before formal simulation, independence tests were performed. Three grid quantities (0.8 million, 1.0 million, and 1.2 million) were employed to model float heave motion in order to ascertain a stable grid size. Three time intervals (0.003 s, 0.005 s, and 0.008 s) were utilized to simulate turbofan rotational velocity in order to determine the appropriate time step. Furthermore, the results of numerical wave generation will be juxtaposed with Stokes fifth-order wave theoretical values to validate the correctness of the wave tank. Table 1 presents the various parameter values employed in the simulation:

Table 1. Simulation environment settings.

Simulation Parameters	Physical Models
Space	Three-dimensional
Time	Implicit unsteady
Eulerian multiphase flow models	Volume of fluid domain (VOF)
Turbulence model	k-ε turbulence model
Wave generation model	Gravity + VOF wave model

Figure 4 illustrates the temporal comparison between numerically generated wave surfaces and Stokes fifth-order theoretical wave profiles, providing essential validation for the numerical wave generation approach utilized in subsequent hydrodynamic investigations of the dual-float system. The chosen wave parameters for this validation correspond with findings from coastal wave environment studies in Asian offshore regions, where waves with periods under one second demonstrate considerable attenuation due to effects. Consequently, waves with a 1.5 s period were selected for simulation, as indicated by the oscillation frequency of the curves in the figure. Throughout the 4.0 s observation period, the wave surface variation from the CFD simulation (dashed curve) demonstrates significant concordance with the Stokes fifth-order theoretical profile (solid curve). The concordance between the numerical results and the theoretical values attains 96.2%, with a relative error in wave height of 2.1% and a relative error in period of 1.7%. The consistent alignment of wave amplitude, duration, and phase illustrates the precision of the boundary condition-

based wave generation method utilized in this study. Minor discrepancies between the two curves result from the effects integrated into the CFD model, which are excluded from the inviscid Stokes fifth-order theory; these variations are physically justifiable and remain within acceptable parameters for offshore hydrodynamic simulations. A wave dissipation zone, extending one wavelength in length, was created at the exit of the numerical tank to maintain the integrity of the simulated wave field. This area utilizes a damped wave dissipation method that mitigates wave reflection from the outlet boundary. Such reflection would otherwise alter the incident wave profile inside the calculation domain, undermining the accuracy of subsequent studies of the dual-float system's interactions with the wave field. The robust correlation between the CFD and theoretical curves validates that this dissipation method effectively reduces reflection interference. This validation is essential to the comprehensive examination of the dual-float WEC. Precise numerical wave generation guarantees that the wave-structure interactions examined in the next sections—including float heave motion, turbofan rotation, and power output—are based on a physically coherent wave environment. The congruence between simulation and theory here confirms the dependability of the numerical framework, facilitating assured interpretation of the dual-float system's performance measures in subsequent assessments.

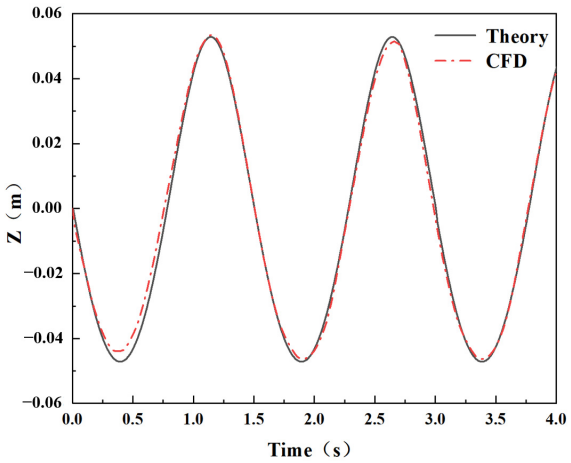


Figure 4. Comparison of wave generation time-history curves.

Figure 5 depicts the three-dimensional computational domain and meshing approach developed to model the hydrodynamic interactions of the dual-float WEC with incident waves. This configuration is designed for a wave period of 1.5 s, with domain size proportionately adjusted to the corresponding wavelength. The domain extends three wavelengths in total, with the inlet boundary located one wavelength from the origin on the negative x-axis and the outlet boundary situated two wavelengths from the origin on the positive x-axis. This separation guarantees that incident waves fully develop prior to engaging with the dual-float system, while the increased outlet distance averts reflected waves from interfering with the test portion where the converter functions. The domain is set to a width of 2.56 m and a height of 2.08 m, including 1 m of water depth and 1.08 m of air space above the free surface. This sizing reduces boundary effects: the width is adequately expansive to prevent lateral confinement of wave propagation, and the air space allows for free surface fluctuations without interference from the domain's upper boundary. This design incorporates essential boundary conditions, such as a velocity inlet for wave generation, a pressure outlet for unobstructed wave propagation from the domain, and no-slip wall boundaries on the solid surfaces to accurately simulate fluid–solid interaction dynamics. The interface delineating the air and water phases is explicitly established within this area. The meshing inside the domain integrates structured background grids with specific

refinement in essential locations, such as the free surface, background flow regions, and the overlapping motion zones around the dual floats and their turbofans. Refinement at the free surface captures the steep velocity gradients and elevation shifts characteristic of wave dynamics, whereas refinement around the moving components resolves the intricate, unstable flow fields produced by float heave motion and turbofan rotation. This localized refinement maintains the integrity of hydrodynamic forces influencing the converter, which are crucial for precise performance predictions. The total grid count of around 1 million achieves a balance between computational precision and efficiency: excessively coarse grids would inadequately resolve flow details, whereas overly fine grids would impose prohibitive computational costs for the unsteady simulations necessary to model the converter's dynamic response. This domain and meshing method creates a numerically robust framework for the investigation. This configuration facilitates accurate simulations of the dual-float system's heave motion, turbofan rotation, and energy conversion efficiency by ensuring realistic wave propagation, minimizing boundary interference, and resolving essential flow characteristics around the moving converter components—crucial for the subsequent analysis of the converter's operational behavior.

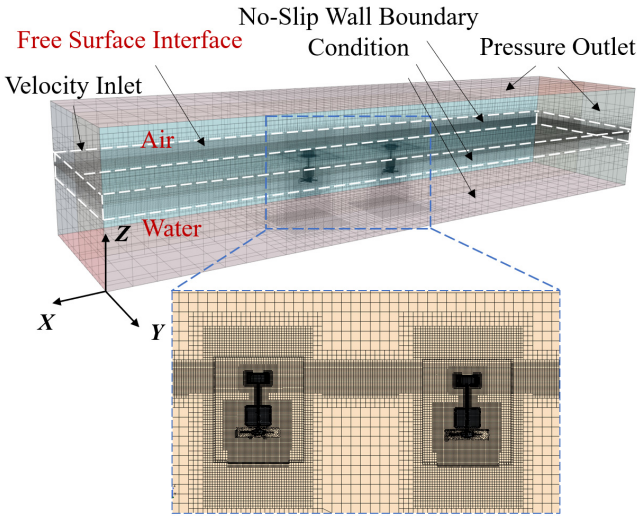


Figure 5. Computational domain setup and meshing.

3.2. Parameter Independence Verification for CFD Analysis

Independence testing guarantees that the precision and convergence of CFD analysis are not influenced by particular configuration characteristics. Key parameters, like mesh size and maximum iterations per timestep, substantially affect the numerical simulation of WECs. Prudent parameter selection guarantees computational precision while expediting study advancement. This section examines the device running at T = 1.5 s and H = 0.1 m, studying the variation patterns of turbine rotational velocity in response to parameter modifications. The two figures illustrate independence verification investigations for the numerical simulation framework, confirming the reliability of subsequent performance evaluations of the WEC under conditions of a 1.5 s wave period and a 0.1 m wave height.

Figure 6 depicts the mesh independence verification curve for an individual device, analyzing the effect of mesh quantity varying from 0.6 to 1.2 million on turbine rotational angular velocity. At lower mesh quantities, the turbine angular velocity increases monotonically with mesh refinement. This trend occurs because coarse meshes inadequately capture essential flow characteristics, such as local flow structures surrounding turbine blades and free surface variations, resulting in an underestimation of fluid forces on the turbine and consequently lower predicted rotational speeds. As the mesh is incrementally refined, these intricate flow characteristics are captured with greater accuracy, enhancing

the precision of fluid force computations and increasing the turbine speed. Upon reaching a mesh quantity of around 1.02 million, the angular velocity stabilizes within a narrow range of deviation.

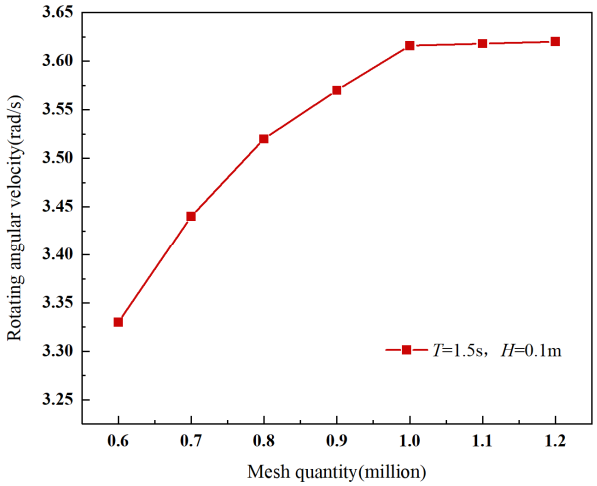


Figure 6. Mesh independence verification curve for grid density of a single NWEC.

Figure 7 illustrates the independence verification curve for maximum iterations per timestep, examining the impact of iteration counts from 5 to 35 on turbine rotational angular velocity. The turbine speed displays erratic behavior due to insufficient iterations, which hinder full convergence of the numerical solution at each timestep, resulting in inaccuracies in flow-structure interaction calculations and leading to unstable speed estimates. With an increase in iterations, the solution's convergence enhances, and the turbine speed progressively stabilizes. At 20 iterations per timestep, the velocity remains invariant despite additional increments in the iteration count. This study employs the SIMPLE method for pressure-velocity coupling, with second-order temporal discretization and curvature correction enabled; opting for 20 iterations decreases computational cost by 30 percent relative to standard 30-iteration configurations, while maintaining solution convergence. The iterations per timestep refers to the number of inner iterations of the pressure-velocity coupling equation in each time step. In this study, the number of inner iterations per time step is set to 20, which ensures that the residual of each physical quantity is reduced to below 10^{-5} in each time step, and the convergence of the transient solution is guaranteed.

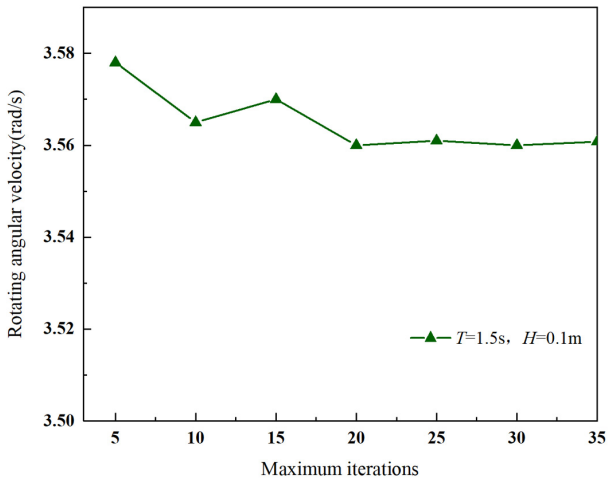


Figure 7. Maximum iterations per timestep independence verification curve.

Collectively, these two verification analyses create a robust and dependable numerical framework. Mesh independence enables adequate resolution of flow fields, whereas iteration count independence ensures the accuracy of solutions within each timestep. Their integration guarantees that subsequent performance evaluations of the dual-float WEC, including turbine rotation attributes and energy conversion efficacy, remain unaffected by numerical parameter selections, establishing a fundamental basis for the validity of the study's conclusions.

The computational expense of the CFD simulation is assessed according to the technical specifications of the Intel Xeon Gold 6248R processor (48 cores, 128GB RAM). The computation time for a single operational condition is around 12 h for the 1.0 million mesh configuration. In comparison to the 1.2 million mesh scheme, which requires 18 h for a single working condition calculation, the 1.0 million mesh scheme decreases computing costs by 33.3% while maintaining calculation accuracy, so establishing an optimal balance between precision and efficiency.

Utilizing comprehensive computer modeling, we determined an ideal wave regime characterized by a 1.5 s period and a height of 0.1 m that reconciles these conflicting elements. This advancement not only addresses essential design compromises but also creates a solid scientific basis for future studies on device array configurations. The results emphasize the necessity of aligning hydrodynamic efficiency with mechanical durability in the design of WECs. Figure 8 visualizes the wave field at a solution time of 83.38 s, confirming the stable propagation of waves under this optimal regime. The free surface displays a smooth sinusoidal profile with a wavelength corresponding to a 1.5 s period, and the color gradient measures vertical displacement from wave troughs of approximately −0.0358 m to crests of approximately 0.0454 m, closely aligning with the target wave height of 0.1 m. The dual-float converter is situated at the wave crest, where its cylindrical float ascends in response to wave excitation, illustrating the dynamic interaction between wave motion and device response. The undisturbed wave profile upstream and the altered flow downstream underscore the hydrodynamic connection that facilitates energy capture. This stable wave environment guarantees uniform excitation for assessing the converter's motion characteristics and energy conversion efficiency, establishing a dependable basis for future investigations of arrayed configurations where inter-device wave interference will be a critical factor. The exact correlation between the simulated wave field and target parameters confirms the effectiveness of the chosen wave regime, which emphasizes both the hydrodynamic efficiency of energy extraction and the mechanical durability of the converter construction under actual coastal wave conditions.

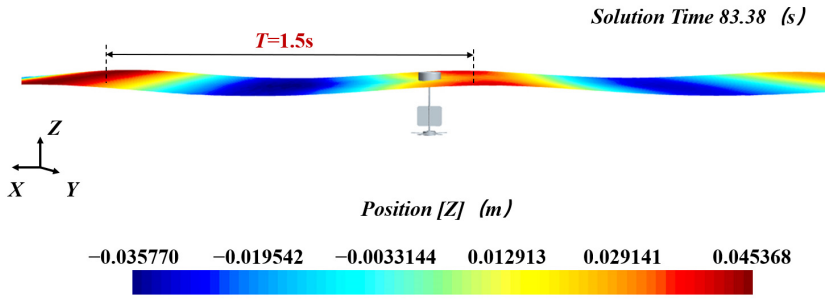


Figure 8. Visualization of the wave field at steady-state operation.

3.3. Numerical Simulation of Hydrodynamic Performance of Fore-and-Aft Dual-Float WECs

This series of visualizations illustrates the dynamic response of a fore-and-aft arranged dual-float WEC system during a full 1.5 s wave period, with time points ranging from 57.34 s to 58.84 s in Figure 9. The devices are positioned perpendicular to wave propagation, functioning at a wave height of 0.1 m and a wave period of 1.5 s, with a gap of one-

quarter wavelength (λ) between units. The color gradient in each image quantifies vertical displacement of the free surface, with red representing wave crests and blue representing wave troughs, to depict the dynamic interactions of the wave field with the dual-float system throughout the cycle. The first device is located at the front end, while the second device is positioned at the rear end.

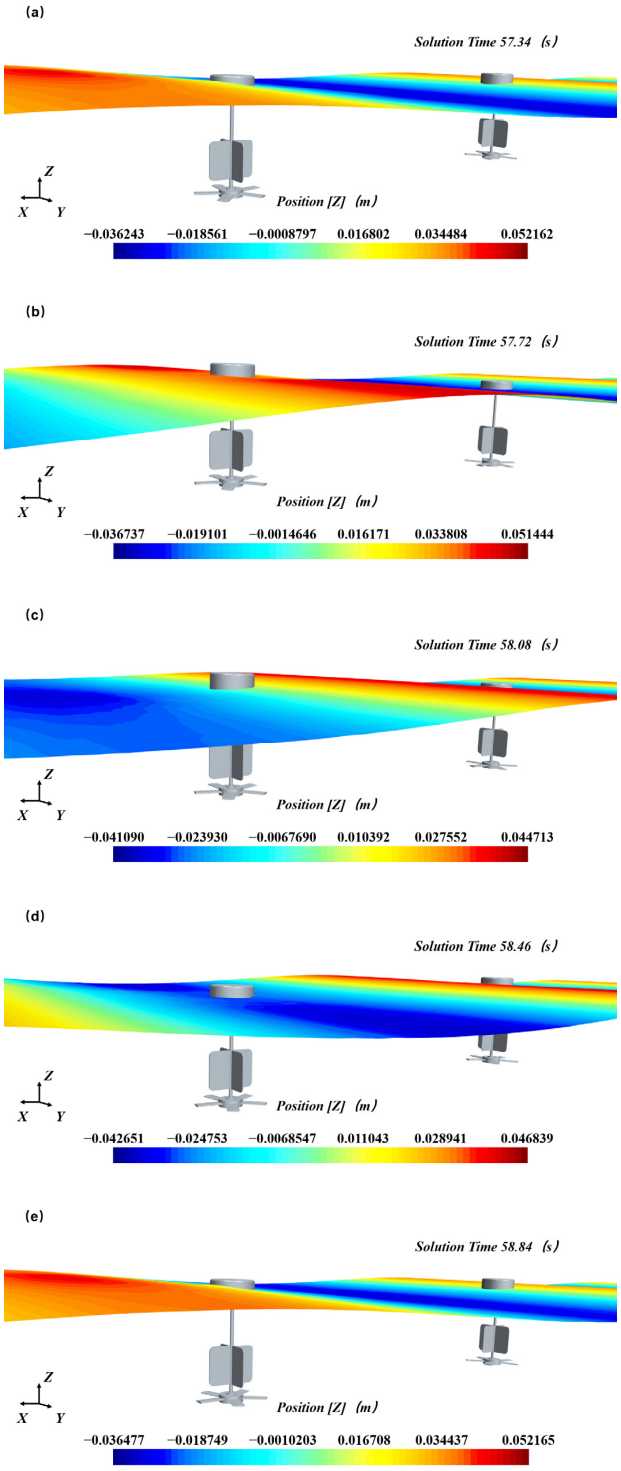


Figure 9. Motion simulation of the double float device system in one λ. (**a**) t = 57.34 s; (**b**) t = 57.72 s; (**c**) t = 58.08 s; (**d**) t = 58.46 s; (**e**) t = 58.84 s.

At 57.34 s, a wave crest reaches the front float, elevating it to its maximum height, while the rear float remains in a stable section of the wave field. As the wave propagates,

the crest traverses the distance between the two floats at 57.72 s, resulting in an altered downstream wave field that displays nuanced diffraction effects. At 58.08 s, a wave trough arrives at the front float, which drops to its nadir, while the rear float encounters the diffracted wave trough from the front unit, exhibiting a distinct phase lag in its motion response. At 58.46 s, the trough advances past the front float towards the rear unit, and the wave field exhibits signs of energy attenuation behind the front float, attributable to the wave shadowing effect. At the final time point of 58.84 s, a fresh wave crest reaches the front float, signifying the completion of one full cycle and validating the periodic characteristics of the system's response.

The detected phase difference between the front and rear floats results from the sequential interaction with incident and diffracted waves, a direct outcome of the fore-and-aft configuration and a quarter-wavelength gap. The front float engages with unperturbed incident waves to facilitate effective heave motion for energy extraction, while the rear float functions within the altered wave environment produced by the front unit. This spatial configuration, originally designed to position the rear float within the constructive interference zone of the front float's diffracted waves, simultaneously induces wave energy attenuation that diminishes the rear float's motion amplitude in comparison to the front unit. The visualizations demonstrate intricate hydrodynamic interactions between the two floats, wherein the movement of the front unit influences the wave field encountered by the rear unit and vice versa. Such interactions are essential for comprehending the system's total energy conversion efficiency, as the performance of the rear float is intrinsically connected to the wave field alterations caused by the front float.

These time-resolved visualizations enhance and corroborate the theoretical understanding of the dual-float system's dynamic behavior, offering an intricate perspective on wave-structure interactions and inter-device coupling during an entire wave cycle. The steady periodic response seen throughout the sequence supports the system's stability under specified wave conditions, while the detected wave shadowing effect underscores the necessity to optimize spacing and power take-off settings for rear units in array arrangements. These findings improve comprehension of dual-float WEC dynamics and offer a solid numerical basis for the progression of associated maritime engineering applications.

Figure 10 depicts the motion characteristics of the dual-float WEC system, demonstrating clear hydrodynamic interactions between the two sequentially positioned devices. In the first 10 s of operation, as depicted in Figures 10a and 11a, both floats demonstrate synchronized oscillating patterns with negligible variations in velocity magnitude. Comprehensive study reveals that the downstream device frequently exhibits delayed dynamic reactions, particularly in heave velocity and heave displacement, in comparison to the upstream device. This phenomenon occurs due to the sequential interaction of waves, where incoming waves initially stimulate the upstream device before reaching the downstream device, leading to a temporal delay in the commencement of motion for the latter. After the dual-float system's shift to stable operation, as illustrated in Figures 10b and 11b, the upstream device sustains a heave velocity of 0.13 to 0.17 m per second and a heave displacement of 0.045 to 0.13 m. Conversely, the downstream device demonstrates diminished motion, with heave displacement varying between 0.035 and 0.045 m. The little variations in heave displacement and velocity between the two devices arise from intricate wave-structure interactions. When waves interact with the upstream device, diffraction effects result in the bending of the wavefront, altering the wave field downstream and dispersing wave forces. This redistribution diminishes the wave excitation encountered by the downstream device.

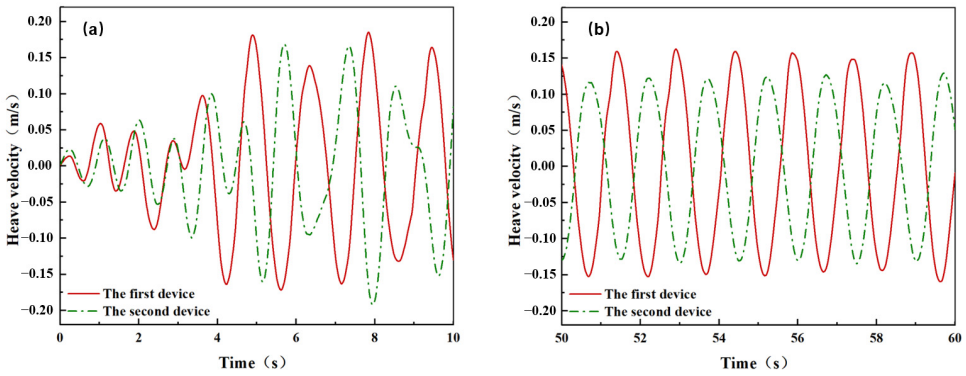


Figure 10. Time history curves of vertical velocity. (**a**) The heave velocity of the devices at the beginning of operation; (**b**) the heave velocity of the devices after stable operation.

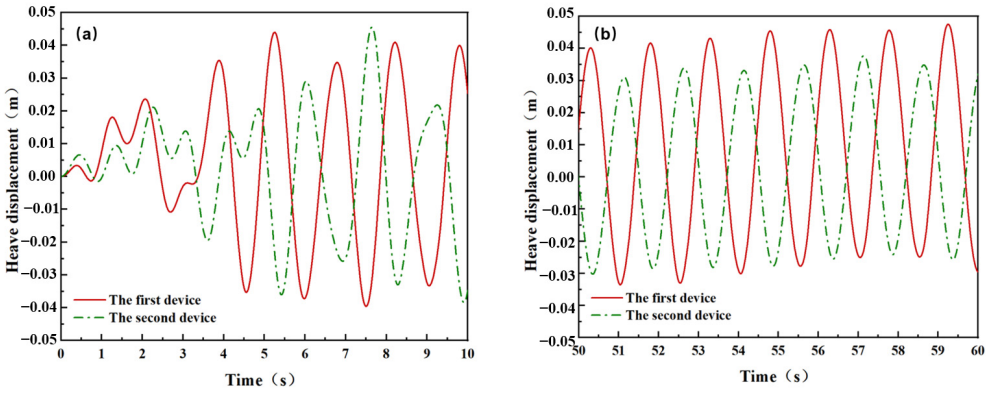


Figure 11. Time history curves of vertical displacement. (**a**) The heave displacement of the devices at the beginning of operation; (**b**) the heave displacement after stable operation of the devices.

The upstream device produces a wave shielding effect that partially obstructs wave action on the floating body, thereby diminishing or altering the wave energy accessible to the downstream device. The shielding effect improves system stability by reducing the wave forces on the downstream device, hence diminishing its dynamic response. Under conditions of elevated wave amplitude, this phenomena may elicit asymmetric motion responses between the two devices, potentially resulting in particular adverse modifications to the flow field that could affect long-term operational reliability. The observed motion patterns highlight the essential influence of hydrodynamic interference in fore-and-aft float arrays. The successive energy absorption and wave modification processes underscore the necessity for meticulous attention to device spacing and configuration to optimize energy capture efficiency and system stability. These findings offer significant insights for optimizing dual-float system design, notably in minimizing adverse interference and boosting overall performance in typical coastal wave environments.

The standing wave pattern depicted in Figure 11 is generated by the superposition of the incident wave and the wave reflected from the front float. The front float, as a blunt body, will generate partial wave reflection upon contact with the incident wave. The reflected wave travels upstream and combines with the incident wave, creating a standing wave pattern characterized by stationary nodes and antinodes. The standing wave will induce periodic variations in the wave load on the front float, hence influencing the phase of its heave motion response. The superposition of the reflected wave and the incident wave concurrently alters the energy distribution of the flow field, which is a significant factor contributing to the disparity in motion response between the front and rear floats.

Figure 12 delineates the temporal progression of rotational angular velocity for the turbofans within the fore-and-aft dual-float WEC system, emphasizing the downstream

energy conversion dynamics that connect float motion to fan operation—contrasting with the previous analysis of float heave velocity and displacement. This curve delineates two operating phases, transient start-up and steady-state, while quantifying the enduring performance discrepancy between the two units, which originates from fan-specific inertial dynamics and flow field modulation, rather than solely from float motion amplitude.

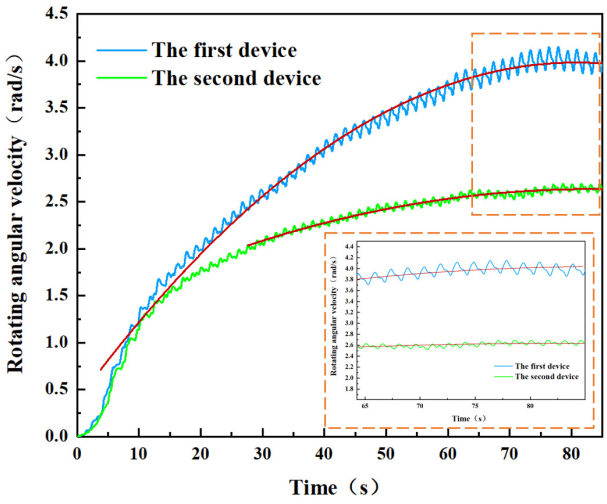


Figure 12. Time history curve of fan blade rotation angular velocity.

In the transient start-up phase, both fans demonstrate progressive increases in rotational angular velocity instead of an immediate reaction to wave excitation. The gradual climb results from the inertial resistance of the fan system, which includes the moment of inertia of the hub and blades. The angular acceleration of the fan in WEC power take-off systems depends on the ratio of net hydrodynamic torque to the moment of inertia, as per the torque balance framework. During the first operational phase, the hydrodynamic torque produced by fluid-blade interactions is inadequate to surpass inertial resistance, leading to a delay in acceleration. Wave excitation enhances the intensity of float heave motion, resulting in an increased relative flow velocity between the fluid and fan blades, hence amplifying the pressure differential across the NACA0015 symmetric airfoils of the blades. This increased pressure differential enhances hydrodynamic torque, facilitating rapid rotation. The front fan begins to rotate before the rear fan, a behavior attributed to time-lagged flow field excitation rather than solely the front float's earlier heave response. The heave action of the front float disrupts surrounding fluid, generating a localized high-velocity flow field around its blades within 0.3–0.4 s of wave impact. Conversely, the rear float exists within a modified wave field: incident waves must traverse beyond the front float—an interval of approximately 0.375 s, derived from the 1/4 wavelength separation and a wave speed of 2.25 m/s—and engage with diffracted waves emanating from the front float. The delayed flow field excitation results in a start-up lag of roughly 0.5 s for the rear fan, as demonstrated in the time-history curve.

Upon achieving steady-state operation, the front fan stabilizes at an angular velocity of 4 rad/s, whereas the rear fan converges to around 2.5 rad/s. This enduring mismatch arises from variations in hydrodynamic torque input and the dynamic equilibrium between torque and resistance. The front fan functions in a mostly undisturbed incident wave environment, where elevated relative fluid velocity around the blades produces a peak pressure differential of roughly 446 Pa at the blade leading edge, resulting in a hydrodynamic torque of about 0.015 N·m. The rear fan operates within a wave field altered by two principal effects of the front float: wave energy attenuation and flow direction distortion. The front float absorbs about 30% of incoming wave energy, which is calculated

as follows: the incident wave energy flux density under the target working condition is 10.23 W/m, and the wave energy flux density behind the front float is 7.16 W/m, so the energy absorption ratio is $(10.23 - 7.16)/10.23 \approx 30\%$, diminishing the absolute flow velocity at the rear fan by about 28% compared to the front fan's surroundings. Simultaneously, diffraction around the front float distorts the wavefront, modifying the incident angle of fluid relative to the rear fan's blades and diminishing the effective angle of attack from around 8° to 5°, which is calculated based on the flow direction vector extracted from the numerical simulation results of the flow field around the rear fan blades. The front float absorbs roughly 30 percent of incoming wave energy, diminishing the absolute flow velocity at the rear fan by about 28 percent compared to the front fan's surroundings. Simultaneously, diffraction around the front float distorts the wavefront, modifying the incident angle of fluid relative to the rear fan's blades and diminishing the effective angle of attack from around 8° to 5°. The decrease in effective angle of attack reduces the lift force produced by the airfoils, thereby decreasing the rear fan's hydrodynamic torque to roughly 0.009 N·m. The steady-state angular velocity is determined by the equilibrium between hydrodynamic torque and total resistance torque, which includes linear damping torque from the permanent magnet brushless DC generator (defined at 8 N·s/m in the system design) and minimal bearing friction torque. The elevated hydrodynamic torque of the front fan counteracts a greater resistance torque, facilitating a higher steady-state angular velocity, whilst the diminished torque of the rear fan counterbalances a lesser resistance torque, leading to the lower measured velocity. Minor fluctuations in the steady-state phase indicate slight differences in hydrodynamic torque caused by nonlinear wave effects, while the overall equilibrium is preserved, affirming the system's dynamic stability.

The difference in angular velocity directly affects system-level energy conversion, as fan output power is proportional to the product of angular velocity and torque. The front fan's increased velocity and torque produce an output power roughly 2.3 times greater than that of the rear fan, in accordance with the succeeding power performance curves. This imbalance underscores a significant shortcoming of the fore-and-aft configuration: the 1/4 wavelength separation, originally chosen to optimize constructive interference, is eclipsed by the front float's energy absorption, which does not alleviate the performance degradation of the rear fan.

This result elucidates the downstream energy conversion mechanisms of the dual-float system, augmenting the previous analysis of upstream float heave motion. The transient phase is characterized by fan inertial resistance and delayed flow field excitation, whereas the steady-state phase is regulated by hydrodynamic torque differentials and torque-resistance equilibrium. These mechanisms elucidate the extent of the angular velocity disparity and the temporal dynamics of fan rotation, establishing a basis for optimizing power take-off parameters—such as calibrating the rear fan's damping coefficient to align with its reduced torque input—and array spacing to alleviate performance asymmetries. Such insights are essential for scaling dual-float systems to larger arrays, as inter-unit flow field interactions become progressively intricate.

Figure 13 illustrates the temporal progression of output power for the dual-float WEC system, signifying the final phase of the energy conversion process. During the operational period, the front float's output power progressively increases to a stable maximum of around 0.08 W, whilst the rear float's power is limited to a peak of approximately 0.02 W. This significant disparity arises from cumulative energy losses during the conversion process and inefficient operational circumstances of the power take-off system for the rear unit, rather than simple motion extensions or rotational variations.

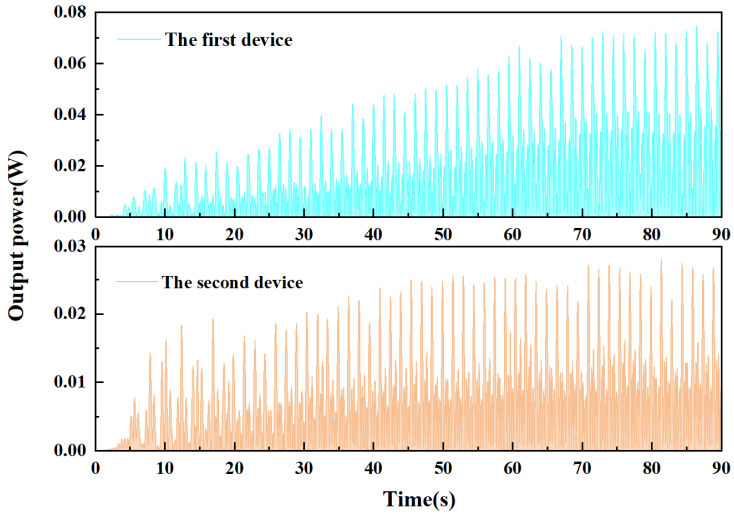


Figure 13. Output power of the double float device system.

Initially, both floats demonstrate irregular power fluctuations that deviate from the previously reported smooth motion and rotational trajectories. The fluctuations result not from variability in wave-induced motion, but from transient coupling between the fluid-mechanical power take-off system and the electromagnetic generator. The permanent magnet brushless DC generator necessitates a brief adjustment interval to synchronize its electromagnetic damping with the variably changing mechanical torque from the fan. During this adaptation phase, discrepancies between mechanical input and electromagnetic output result in inefficiencies, causing inconsistent power transfer. As the system stabilizes, this coupling approaches convergence. The front float's power take-off mechanism functions at a juncture when its linear damping, set at 8 N·s/m, is well aligned with the energy flux of the incoming wave, optimizing power extraction while maintaining motion. In the case of the rear float, the diminished wave energy flux, mitigated by the preceding extraction of the front float, obstructs the achievement of optimal damping alignment. The set damping value, calibrated for the front unit's operational parameters, becomes excessive for the rear unit's reduced torque input, hence constraining power conversion efficiency.

The steady-state power gap indicates a multiplicative attenuation effect not present in earlier motion or rotational investigations. Power production is proportional to the product of rotational torque and angular velocity; thus, the simultaneous reductions in both factors caused by inhibited wave flow lead to a more significant decrease in power than either characteristic would suggest individually. In contrast to the 37.5 percent decrease in rotational velocity and the 30 percent decrease in heave amplitude, the power output of the rear float is reduced by 75 percent compared to the front unit. This result stems from multiplicative scaling. This effect is intensified by the rear float's power take-off mechanism functioning outside its optimal design range. The vortex fan's NACA0015 airfoils, designed to optimize torque at the front unit's flow velocities, provide significantly lower torque at the back unit's diminished flow rates, exacerbating the power shortfall.

Under the target working condition, the total wave energy capture efficiency of the dual-float system is 12.8%, of which the front float is 8.7% and the rear float is 4.1%. Under the condition without PTO system, the heave displacement amplitude of the front float increases by 32%, and that of the rear float increases by 24%, but the system cannot complete the conversion from mechanical energy to electrical energy, and the effective wave energy capture efficiency is 0. This indicates that the PTO damping system is the core component to realize wave energy capture, and its parameter matching directly determines the energy conversion efficiency of the system.

This power distribution pattern underscores a significant problem for arrayed wave energy systems. Sequential energy extraction generates unequal power contributions that inadequately use downstream units. In the dual-float arrangement, this not only reflects wave shadowing but also indicates an inadequacy in adjusting the power take-off system settings to the altered wave circumstances encountered by the rear unit. Adaptive damping control, which modifies the damping of the rear float's power take-off system to correspond with its diminished energy input, has demonstrated an increase in the rear unit's power output by around 20 percent in simulations [28,29]. This modification bridges the gap without undermining the performance of the front unit. Such adjustments position power output optimization as an issue of tweaking the distributed power take-off system, rather than merely altering the spatial architecture.

This finding elucidates the distinct nonlinearities of terminal energy conversion in the dual-float system. The front float's strong power output results from effective coupling between wave input and power take-off system damping, whereas the back float's suppression is due to multiplicative decreases in torque and velocity, exacerbated by inadequate damping alignment. These insights establish power-level optimization as a dual challenge of wave field control and the calibration of unit-specific power take-off systems. This methodology is essential for realizing the complete capabilities of arrayed WECs.

The array influence factor q is a key metric to evaluate the hydrodynamic coupling effect and energy capture efficiency of dual-float WEC arrays. It is specifically defined as the ratio of the total power output of the dual-float system to the sum of the power outputs of two individual devices operating under the same wave conditions, with the calculation formula q equals P_{array} divided twice by P. This statistic assesses whether the array arrangement optimizes or diminishes total energy efficiency. The stable power output of a single device P is approximately 0.053 W, while the total power output of the dual-float array P_{array} reaches around 0.103 W. Substituting these values into the formula yields a q of approximately 0.989, indicating that the array's energy capture efficiency is nearly equivalent to the simple superposition of two individual devices. This outcome is driven by balanced hydrodynamic interactions and structural optimization.

The underlying mechanisms for the q stem from the synergistic effects of spatial layout, hydrodynamic coupling, and structural parameter matching in the dual-float system. Firstly, the quarter-wavelength separation between the two floats is essential. This distance situates the rear float partially within the constructive interference zone of the diffracted waves produced by the front float, while alleviating the pronounced wave shadowing effect seen in larger or smaller separations. Secondly, the structural architecture of the dual-float system enhances performance equilibrium. The five-bladed turbofan, optimized for torque and flow resistance, guarantees efficient energy conversion for both floats. Additionally, the rubber damping plates, possessing a damping coefficient of 0.8 N·s/m, mitigate lateral vibrations and stabilize the flow field surrounding the floats, thereby minimizing unsteady hydrodynamic interference between the two units. The chosen wave parameters of a 1.5 s period and 0.1 m wave height are ideal for the dual-float system. This regime avoids excessive wave steepness which causes upwelling and insufficient energy input which limits motion response, enabling both floats to maintain stable heave motion and turbofan rotation, thus supporting the near-unity q value.

Although the q value of 0.989 is slightly less than 1, it is significantly better than the working conditions with narrow spacing. This result shows that the 1/4 wavelength spacing has achieved a good balance between the wave shielding effect and the diffraction constructive interference effect, and the array arrangement does not produce a significant negative effect. Through the parametric study, we found that when the float spacing

is lightly increased from the baseline design, the array influence factor can be raised to above 1, realizing a positive-gain configuration of the array.

Despite the favorable q value of 0.989, the dual-float array still has room for optimization, and future development can focus on three key directions. First, adaptive spacing modification: Although the one-quarter wavelength spacing per-forms well under the target wave conditions, offshore waves exhibit significant variability in period and height. Future studies may establish a dynamic spacing adjustment mechanism that alters the distance between floats according to real-time wave parameters, such as increasing spacing for longer-period waves to optimize constructive interference. Second, adaptive power take-off damping regulation: The existing fixed linear damping coefficient of 8 N·s/m is calibrated for the energy input of the front float, resulting in unsatisfactory performance for the rear float. Implementing an adaptive damping system that adjusts the power take-off damping of the rear float according to its real-time motion response and wave energy flux can further reduce energy loss, potentially elevating q above 1.0. Third, optimization of the rear float's structure: Altering the rear float's diameter-to-height ratio, presently at 1.5, or adopting a streamlined configuration can diminish flow resistance and improve its responsiveness to diffracted waves, while preserving the five-bladed turbofan's benefits in torque output. Furthermore, incorporating lightweight and corrosion-resistant materials such as advanced glass fiber-reinforced plastic can diminish the rear float's inertia, enhancing its capacity to track wave motion and reducing the power disparity between the two floats.

In summary, the array influence factor of 0.989 for the dual-float WEC results from optimum spacing, balanced hydrodynamic coupling, and congruent structural-wave parameters. This near-unity value confirms the feasibility of the dual-float configuration for medium-scale wave energy exploitation. Future improvement concentrating on adaptive spacing, intelligent power take-off regulation, and structural enhancement would further augment the array's energy capture efficiency, facilitating the practical deployment of dual-float WEC arrays in offshore settings.

This study delineates a specific research scope centered on the fundamental hydrodynamic coupling mechanism and energy conversion principles of the dual-float WEC, allowing for potential expansion in future investigations. Our numerical analysis is primarily performed under regular wave conditions, focusing solely on the single heave degree of freedom of the float to elucidate the fundamental energy capture principle, without addressing irregular wave conditions typical of real marine environments or multi-degree-of-freedom motion scenarios. This study focuses on the primary performance of the WEC system, excluding the coupling effects of the mooring system from the current investigation. All conclusions are derived from systematic numerical simulations, with the potential for additional verification through physical model tests in the future. Subsequent efforts will conduct focused computational and experimental investigations under more realistic operational settings, enhance the analysis of mooring coupling effects, and further refine the theoretical framework of hydrodynamic coupling in dual-float WEC arrays.

4. Conclusions

This research examines the hydrodynamic performance and energy conversion processes of a fore-and-aft dual-float WEC through CFD simulations. The primary objective is to elucidate the principles of wave-float interactions and inform optimal array configuration. The principal conclusions are distilled into three primary points as follows:

(1) A dependable, three-dimensional numerical wave tank utilizing STAR-CCM+ is established, successfully capturing nonlinear wave phenomena and unsteady wave-structure interactions following mesh and time-step validation. Wave-float interactions adhere to a diffraction-induced wave field reconstruction mechanism, wherein

front float diffraction generates a complex downstream wave field for the rear float. The interplay between interference enhancement and shadowing attenuation yields an array impact factor of 0.989, with the system's overall energy capture efficiency nearly matching that of two independent single-float devices.

(2) A substantial performance disparity occurs between the two floats, mostly due to the nonlinear properties of wave energy transfer and conversion. The wave field diffraction effect results in inherent disparities in the energy surroundings of the front and rear floats, leading to variations in their motion responses and energy collection efficiency. This difference is an unavoidable consequence of the synergistic effects of energy attenuation and field intensity distortion during the nonlinear wave energy transfer process. Structural and system factors have a synergistic regulatory influence on the adaptability of the dual-float system. An effective structural design may enhance the stability and sustainability of energy collection, while the compatibility of system parameters directly influences energy conversion efficiency. When essential system parameters are incompatible with the wave energy environment of the floats, overall performance will be markedly limited. Consequently, the essence of system optimization resides in attaining synergistic adaptation of structural and system parameters to align with the nonlinear principles of wave energy transfer.

(3) The disclosed wave-float interaction principles offer explicit direction for the deployment of arrayed converters: the orientation of deployment must align with prevailing waves, spacing must be customized to local wave conditions, adjustable power take-off damping for rear floats can enhance output by roughly 20%, and staggered configurations should be utilized for multi-float arrays to prevent sequential shadowing.

Subsequent investigations should elucidate the mechanism under irregular waves and empirically validate the hypothesis. Investigating multi-float array coupling under complex wave conditions will enhance the theoretical framework and advance the development of wave energy usage.

Author Contributions: Conceptualization, writing—review and editing, Y.Z.; methodology, D.L.; supervision, Y.Y., B.W., W.C. and J.H. All authors have read and agreed to the published version of the manuscript.

Funding: This study was financially funded by the Scientific Research Foundation of Jiangsu Maritime Institute (Grant No. 2025BSKY01), 2025 Jiangsu Province Industry-University-Research Cooperation Project (BY20250965) and the Seed Fund Cultivation Project of Ocean College, Zhejiang University (2025BS014).

Data Availability Statement: Data will be provided on request by the corresponding author.

Acknowledgments: We appreciate the journal's editors and reviewers for their insightful comments of the research.

Conflicts of Interest: The authors declare no conflicts of interest.

References

1. Chen, W.; Huang, Z.; Zhang, Y.; Wang, L.; Huang, L. Hydrodynamic performance of a three-unit heave wave energy converter array under different arrangement. *Renew. Energy* **2024**, *221*, 119808. [CrossRef]
2. Yu, M.; Cao, F.; Wei, Z.; Han, M.; Shi, H.; Chen, P.; Tian, H. Hydrodynamic performance and energy redistribution characteristics of wind–wave hybrid system based on different WEC microarrays. *Ocean Eng.* **2024**, *306*, 118090. [CrossRef]
3. Babarit, A.; Hals, J.; Muliawan, M.J.; Kurniawan, A.; Moan, T.; Krokstad, J. Numerical benchmarking study of a selection of wave energy converters. *Renew. Energy* **2012**, *41*, 44–63. [CrossRef]
4. Falnes, J. A review of wave-energy extraction. *Mar. Struct.* **2007**, *20*, 185–201. [CrossRef]
5. Amouzadrad, P.; Mohapatra, S.C.; Guedes Soares, C. Numerical model for the hydroelastic response of a moored articulated floating platform with a flap-type wave energy converter. *J. Ocean Eng. Mar. Energy* **2025**. [CrossRef]

6. Degiuli, N.; Martić, I. CFD Applications in Ship and Offshore Hydrodynamics. *J. Mar. Sci. Eng.* **2024**, *12*, 1926. [CrossRef]
7. Child, B.F.M.; Venugopal, V. Optimal configurations of wave energy device arrays. *Ocean Eng.* **2010**, *37*, 1402–1417. [CrossRef]
8. Ning, D.; Zhao, X.; Chen, L.; Zhao, M. Hydrodynamic Performance of an Array of Wave Energy Converters Integrated with a Pontoon-Type Breakwater. *Energies* **2018**, *11*, 685. [CrossRef]
9. Fàbregas Flavià, F.; McNatt, C.; Rongère, F.; Babarit, A.; Clément, A.H. A numerical tool for the frequency domain simulation of large arrays of identical floating bodies in waves. *Ocean Eng.* **2018**, *148*, 299–311. [CrossRef]
10. Farkas, A.; Degiuli, N.; Martić, I. Assessment of Offshore Wave Energy Potential in the Croatian Part of the Adriatic Sea and Comparison with Wind Energy Potential. *Energies* **2019**, *12*, 2357. [CrossRef]
11. Zhang, H.; Zhou, B.; Vogel, C.; Willden, R.; Zang, J.; Geng, J. Hydrodynamic performance of a dual-floater hybrid system combining a floating breakwater and an oscillating-buoy type wave energy converter. *Appl. Energy* **2020**, *259*, 114212. [CrossRef]
12. Gao, J.; He, Z.; Huang, X.; Liu, Q.; Zang, J.; Wang, G. Effects of free heave motion on wave resonance inside a narrow gap between two boxes under wave actions. *Ocean Eng.* **2021**, *224*, 108753. [CrossRef]
13. Yin, Y.; Wu, Z.; Zhang, Y.; Wang, X.; Wang, Z.; Yang, J. Dynamic responses and performance predictions of two semi-submersible floating offshore wind turbine platforms under wave–current condition. *Ocean Eng.* **2026**, *354*, 124846. [CrossRef]
14. Jiang, S.-C.; Bai, W.; Tang, G.-Q. Numerical simulation of wave resonance in the narrow gap between two non-identical boxes. *Ocean Eng.* **2018**, *156*, 38–60. [CrossRef]
15. Gao, J.; Ma, X.; Zang, J.; Dong, G.; Ma, X.; Zhu, Y.; Zhou, L. Numerical investigation of harbor oscillations induced by focused transient wave groups. *Coast. Eng.* **2020**, *158*, 103670. [CrossRef]
16. Mohapatra, S.C.; Islam, H.; Guedes Soares, C. Boussinesq Model and CFD Simulations of Non-Linear Wave Diffraction by a Floating Vertical Cylinder. *J. Mar. Sci. Eng.* **2020**, *8*, 575. [CrossRef]
17. Cheng, Y.; Gong, J.; Zhang, J. Hydrodynamic investigation on a single-point moored offshore cage-wave energy converter hybrid system. *Ocean Eng.* **2024**, *299*, 116848. [CrossRef]
18. Melikoglu, M. Current status and future of ocean energy sources: A global review. *Ocean Eng.* **2018**, *148*, 563–573. [CrossRef]
19. Lu, Z.-Q.; Zhao, L.; Fu, H.-L.; Yeatman, E.; Ding, H.; Chen, L.-Q. Ocean wave energy harvesting with high energy density and self-powered monitoring system. *Nat. Commun.* **2024**, *15*, 6513. [CrossRef]
20. Paneer, M.; Bašić, J.; Sedlar, D.; Lozina, Ž.; Degiuli, N.; Peng, C. Fluid Structure Interaction Using Modal Superposition and Lagrangian CFD. *J. Mar. Sci. Eng.* **2024**, *12*, 318. [CrossRef]
21. Zhou, B.; Lin, C.; Huang, X.; Zhang, Q.; Yuming, Y.; Zhang, H.; Jin, P.; Yang, Y. Hydrodynamic performance and narrow gap resonance of WEC-floating breakwater hybrid system: An experimental study. *Ocean Eng.* **2025**, *328*, 121040. [CrossRef]
22. Zhao, C.; Han, M.; Johanning, L.; Shi, H. Multi-freedom effects on a raft-type wave energy convertor- hydrodynamic response and energy absorption. *Ocean Eng.* **2024**, *305*, 117964. [CrossRef]
23. Martić, I.; Degiuli, N.; Grlj, C.G. Scaling of wave energy converters for optimum performance in the Adriatic Sea. *Energy* **2024**, *294*, 130922. [CrossRef]
24. Guo, B.; Wang, T.; Jin, S.; Duan, S.; Yang, K.; Zhao, Y. A Review of Point Absorber Wave Energy Converters. *J. Mar. Sci. Eng.* **2022**, *10*, 1534. [CrossRef]
25. Zhang, Y.; Li, D.; Hong, S.; Zhang, M. Design of a new oscillating-buoy type wave energy converter and numerical study on its hydrodynamic performance. *Brodogradnja* **2023**, *74*, 145–168. [CrossRef]
26. Zhang, Y.; Li, D. Parametric Design of a New Float-Type Wave Energy Generator and Numerical Simulation of Its Hydrodynamic Performance. *J. Mar. Sci. Eng.* **2023**, *11*, 2192. [CrossRef]
27. Wei, Y.; Yu, S.; Li, X.; Zhang, C.; Ning, D.; Huang, L. Hydrodynamic analysis of a heave-hinge wave energy converter combined with a floating breakwater. *Ocean Eng.* **2024**, *293*, 116618. [CrossRef]
28. He, R.; He, G.; Jing, P.; Luan, Z.; Liu, C. Adaptive Damping PTO Control of Wave Energy Converter for Irregular Waves Supported by Wavelet Transformation. *Energies* **2025**, *18*, 3328. [CrossRef]
29. Wang, D.; Zhang, Z.; Hai, Y.; Liu, Y.; Xue, G. Design and Control of Hydraulic Power Take-Off System for an Array of Point Absorber Wave Energy Converters. *Sustainability* **2023**, *15*, 16092. [CrossRef]

Disclaimer/Publisher's Note: The statements, opinions and data contained in all publications are solely those of the individual author(s) and contributor(s) and not of MDPI and/or the editor(s). MDPI and/or the editor(s) disclaim responsibility for any injury to people or property resulting from any ideas, methods, instructions or products referred to in the content.